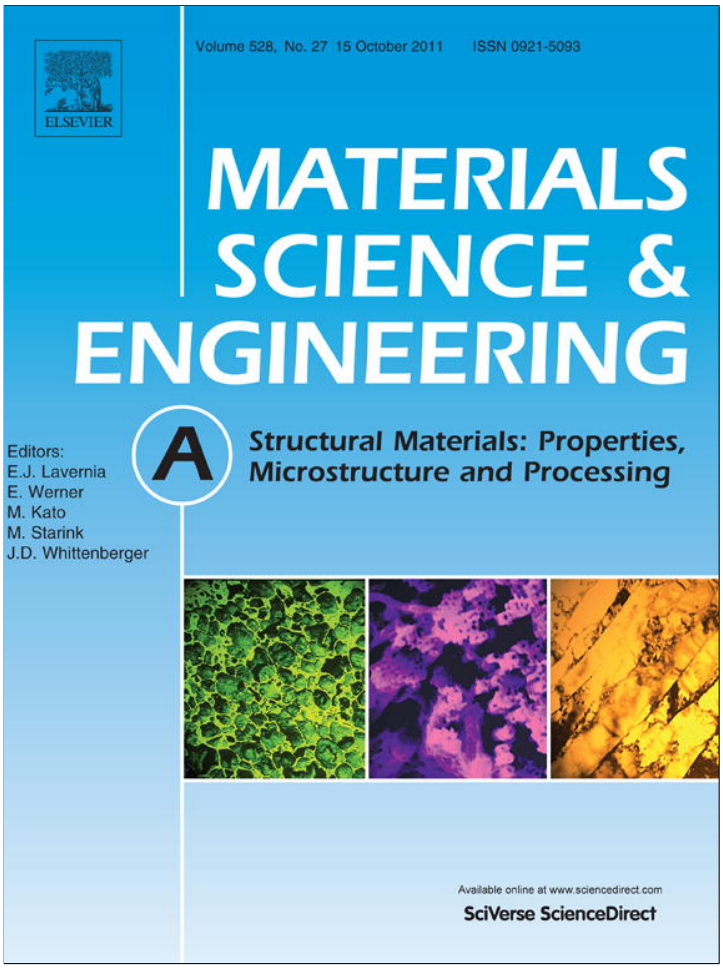

Materials Science and Engineering A 528 (2011) 7857–7866

Contents lists available at ScienceDirect

Materials Science and Engineering A

journal homepage: www.elsevier.com/locate/msea

Deformation characteristics of low carbon steel subjected to dynamic impact loading

W. Visser[a], Y. Sun[a], O. Gregory[b], G. Plume[a], C-E. Rousseau[a], H. Ghonem[a,*]

[a] Department of Mechanical Engineering, University of Rhode Island, Kingston, RI 02881, USA
[b] Department of Chemical Engineering, University of Rhode Island, Kingston, RI 02881, USA

ARTICLE INFO

Article history:
Received 26 November 2010
Received in revised form 19 May 2011
Accepted 23 June 2011
Available online 29 June 2011

Keywords:
Low carbon steel
Shock
Impact loading
Twinning
Post-impact

ABSTRACT

The effects of impact loading on changes in microstructure have been studied in low carbon steel. Low to moderate shock loading tests have been carried out on steel specimens using a single stage gas gun with projectile velocities ranging from 200 to 500 m/s. Stress history at the back face of the target specimen and projectile velocity prior to impact were recorded via manganin stress gauges and velocity lasers, respectively. A Johnson–Cook constitutive material model was employed to numerically simulate the material behavior of low carbon steel during impact and obtain the particle velocity at the impact surface as well the pressure distribution across the specimens as a function of impact duration. An analytical approach was used to determine the twin volume fraction as a function of blast loading. The amount of twinning within the α-ferrite phase was measured in post-impact specimens. A comparison between experimental and numerical stress histories, and analytical and experimental twin volume fraction were used to optimize the material and deformation models and establish a correlation between impact pressure and deformation response of the steel under examination. Strain rate controlled tensile tests were carried out on post-impact specimens. Results of these tests are discussed in relation to the effects of impact loading on the yield and ultimate tensile strength as well as the hardening and strain energy characteristics.

1. Introduction

Impact loading of steel is a subject that has been studied widely for structural applications and material characterization. It has been established that high strain rate loading of steel will result in a change of both microstructural and mechanical properties which individually affect the residual life of the material. Vast amounts of research has been done in order to assess blast loading and deformation effects, much of it being on steel as it is a primary reinforcing phase of structures. Research in blast analysis, while in general utilizes the finite element technique to provide solutions for the dynamic response of the structures [1], requires implementation of microstructure constitutive models required to accurately capture changes in mechanical properties during high strain rate loading.

In order to replicate the pressure profile and high strain rate deformation caused by explosive loading and recover intact specimens suitable for further testing and analysis, various techniques exist of which Field et al. [2] provide a detailed review. Some basic techniques which are of main concern to material characterization are drop weight testing, split Hopkins pressure bar, Taylor impacts, plate impacts, and explosive loading. While SHPB tests produce elastic–plastic wave propagation, the maximum strain rates achieved are typically in the range of 10^4 s^{-1}. Plate impact tests are often used to replicate explosive loading due to the fact that the strain rates, greater than 10^4, and planar shock waves achieved clearly simulate that of explosive shock wave loading. During plate impacts at high velocities, a state of one-dimensional strain is produced until lateral release waves from the edge of the projectile and target specimen reach the center of the impact area. To achieve the highest velocities, above 1 km/s, two and three stage gas guns are used. These techniques are typically used for obtaining Hugonoit curves, measuring spall strength, post-impact mechanical testing, and measuring phase change, the latter of which is the concern of the work presented herein.

An important aspect in the post-impact analysis of materials is the phase change of the microstructure, which is generally incorporated into analytical modeling in order to predict deformation response. Recent studies, by Gregory et al. [3], of recovered pipe bomb fragments provided basis for characterization of plain carbon-steel subject to high rate deformation. They observed metallurgical variations of the steel in order to estimate explosive loading severity. It was found that explosive loading resulted in elongation in grains in both the α-ferrite and pearlite phases, intersecting slip bands and cross slip, as well as mechanical twin

* Corresponding author. Tel.: +1 401 874 2909; fax: +1 401 874 2925.
E-mail address: ghonem@egr.uri.edu (H. Ghonem).

0921-5093/$ – see front matter © 2011 Elsevier B.V. All rights reserved.
doi:10.1016/j.msea.2011.06.069

formation. Firrao et al. [4] subjected stainless steel to plane shock wave loading by means of spherical plastic explosives with varying charge weights and varying charge-target distances. Changes in microstructure on the impact surface included oxidations, partial melting at grain boundaries, isolated slip bands, and mechanical twins in areas around fragment impact points. Changes through the thickness of the specimen were limited to mechanical twins in discontinuous layers bordering the exposed surface, but never across the entire thickness. Through X-ray analysis it was found that dislocation density remains unchanged, proving that deformation by dislocation slip, and subsequently plastic yielding, was not reached, which is also evident through measurement of thickness variations. Based upon observed twinning and estimated explosive pressures, Firrao et al. [4] were able to calculate critical stress required for twinning, and proved that twin nucleation occurs prior to yielding. De Resseguier and Hallouin [5] studied iron disks of different thickness submitted to shock loading by means high-power laser pulses. Post-shock studies of the iron microstructure revealed significant twin formation. Using a constitutive twinning model proposed by Johnson and Rohde [6] accurate predictions of twin volume fraction and elastic–plastic response of the material have been made [5,7]. They used plate impacts to examine shock-loaded iron and analytically predict twin volume fraction in recovered specimens as a function of impact stress. Atroshenko et al. [8] examined the strengthening properties of materials, including copper, aluminum, titanium, and steel, due to spherical loading by means of explosives, and uniaxial loading using a light gas gun. The strength of the material was measured as a function of distance from the impact using microhardness measurements. In all materials except aluminum, microstructure refinement and increases in hardness occurred. Smida and Bosansky [9] provide experimental and fractographical analysis of ferritic structural steel in order to provide a correlation between the role of deformation twins and mode of fracture. Tensile and Charpy impact tests were carried out and the occurrence of deformation twins on the fracture surface were studied. Murr et al. [10] observed profuse mechanical twinning in Tantalum when subjected to shock wave deformation of magnitudes up to 45 GPa. From post-impact testing, shock hardening was observed which have been attributed to twins as barriers to plastic deformation.

Deformation in BCC materials by means of shock loading is described as being composed of the competing mechanisms of slip and twinning. Murr et al. [10] rationalize that critical twinning stress is highly dependent upon and directly proportional to the stacking-fault energy. Their work examined twin formation during shock loading and twinning effect on the post-shock mechanical response of Tantalum. Murr et al. found that twinning was more predominant at the impact surface than at the back surface. Post-shock testing consisted of quasi-static and dynamic compression tests as well as microhardness measurements. The rationale of slip–twinning transition was explained through experimental observations and a mechanistic model proposed by Armstrong and Worthington. A model was presented to predict the critical threshold stress for twin initiation which is based upon the Swegle–Grady relationship, grain-size and temperature. Meyers et al. [11,12] recognize the fact that twin initiation and growth is closely tied to dislocation motion which is highly strain rate and temperature sensitive. They note that twinning can have two significant effects upon plastic deformation; it increases the work hardening rate by creating more barriers, effectively subdividing the grains, and it contributes to plastic deformation due to twinning shear. Meyers briefly describes the effects of strain rate, temperature, grain size, texture, and stress state effects upon twinning nucleation. The model used is based upon a similar theory for FCC material in Murr's study of Tantalum [10], in which dislocation pile-ups are a key aspect to twin nucleation. Equations for critical shear stress for twining are presented for BCC, FCC, and HCP materials, all of which are dependent upon strain rate, temperature, and the Hall–Petch relation for grain size. They describe that the twins per grain is a function of stress which is independent of temperature and strain rate and the amount of twins will increase monotonically with increasing stress. The evident common aspect in all these works is the twin formation in steel during high strain rate loading. A correlation, however, does not exist between blast conditions, i.e. strain rate and stress state, and twin volume fraction, from which a unique criteria defining material integrity can be established. This criterion is the objective of this study. For this purpose, the effect of blast loading up to strain rates of $10^5\ s^{-1}$, on the microstructure deformation mechanisms of low carbon steel will be examined. Discs of low carbon steel were subjected to high velocity impact loading using a light gas gun. Impact specimens were analyzed by measurement of microstructural variations and mechanical properties. Attempts are made to study the deformation pattern in steel using material and deformation models. Results of this analysis are linked with the experimental work in order to assess the validity of the approach. Prediction of impact loading conditions will be achieved through a relationship between twin volume fraction and impact stress history and linked to post-impact mechanical properties. An experimental procedure was used to impact low carbon steel specimens and experimental observations of microstructure. In addition, numerical methods used and means of obtaining accurate results are described. An analytical model of dynamic deformation based upon slip and twinning is described and results are compared with experimental findings.

2. Material and experimental procedure

The as received microstructure of the low carbon steel, as shown in Fig. 1, consists of primarily α-ferrite phase with colonies of pearlite. The pearlite colonies are made of α ferrite and Fe_3C cementite lamellas; Fig. 1. Average grain size is 50 μm with 9% volume fraction of the pearlite phase. Tensile tests of as received material showed yield strength of the material to be 348 MPa at 0.2% offset at room temperature with a Young's modulus of 197 GPa. Preparation of all specimens was done by mechanical polishing to 1 μm and chemical etching using 5% nital solution. This material was prepared into round discs by electro discharge machining and tested by subjecting it to different impact loads using a single stage light gas gun. A series of five plate impact experiments have been carried out using a single stage light gas gun; Fig. 2a. Fixed back conditions, Fig. 2b, were employed in order to minimize energy loss and provide means for recovering post-impact specimens; Fig. 2c provides a schematic of the experimental set up. The projectile measurements are 31.75 mm diameter and 3 mm thick, while the target disk and backing plate

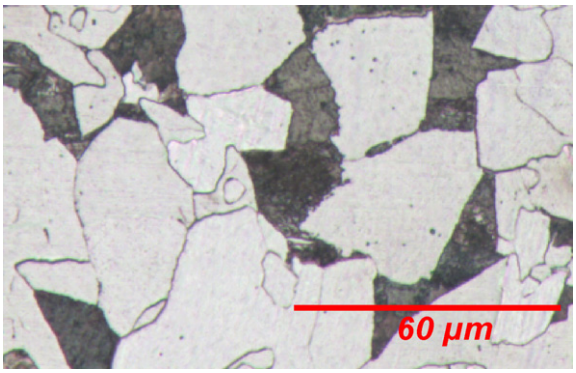

Fig. 1. Optical Micrograph of as received A572 grade 50 structural steel. Lighter grains are α-ferrite, and darker grains are pearlite.

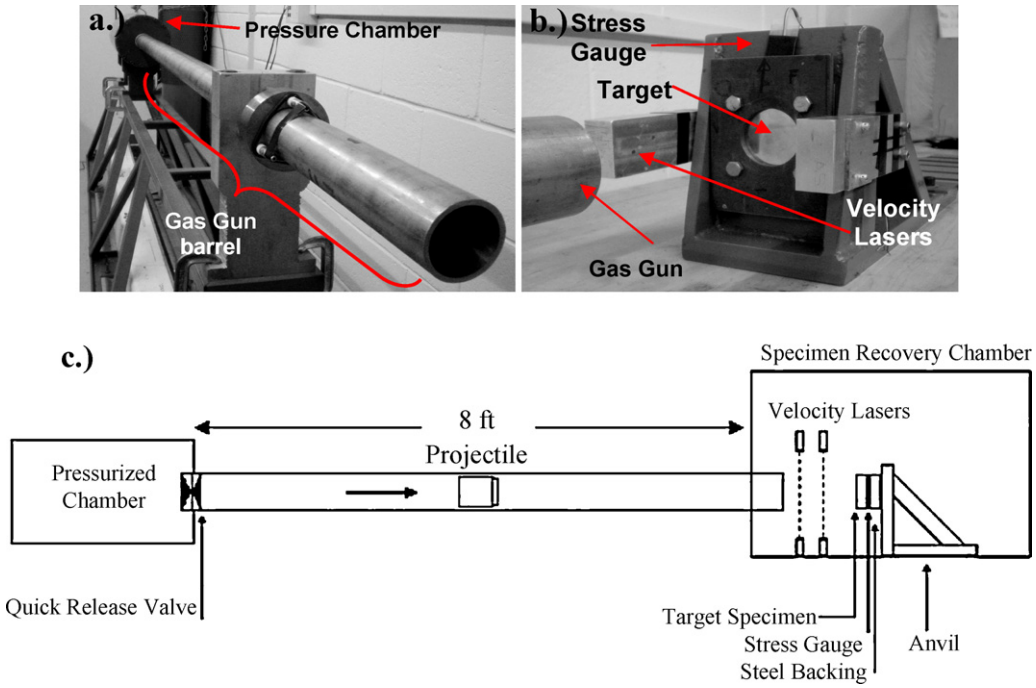

Fig. 2. (a.) Photograph of experimental gas gun. (b.) Fixed back apparatus for plate impact tests. (c.) Schematic of gas gun and target apparatus.

measurements are 57.15 mm diameter and 6 mm thick. The target dimensions allowed for tensile specimens to be machined from deformed specimens for possible mechanical testing.

Projectile velocities ranging from 200 to 500 m/s were measured using two lasers which were mounted perpendicular to the projectile and in front of the target. Input pressure was used to control projectile velocities and magnitude of impact loads. Input pressure of Helium gas was used to control projectile velocities and achievable stress levels. Longitudinal stress histories were recorded using manganin stress gauges bonded centrally between the back surface of the target disk and a steel backing plate.

Typical results of normal stress versus time curves are shown in Fig. 3, for the five different impact velocities. These curves, generated from data recorded from the back surface of the impacted target disk, are characterized by four distinct features; the elastic precursor, the plastic wave, the peak stress level and duration, and the unloading wave. The Hugonoit elastic limit, σ_{HEL}, which is the amplitude of the initial elastic wave, is related to the shear stress, τ, through the relation:

$$\sigma_{HEL} = 2\tau\left[\frac{1-\nu}{1-2\nu}\right] \quad (1)$$

where ν is Poisson's ratio. From the impact stress–time histories, the elastic limit for all curves is reached at 1 GPa. A σ_{HEL} of 1 GPa corresponds to a 0.285 GPa maximum resolved shear stress, and for shear stress greater than this, it is suggested that dislocation slip accommodates plastic deformation [6].

The time between impact and that at which the stress gauge at the back surface begins to register the elastic wave can be estimated using the velocity of the elastic precursor. The wave speed of the elastic precursor, $C_{Elastic}$, is described as [13]:

$$C_{Elastic} = \sqrt{\frac{E(1-\nu)}{\rho(1+\nu)(1-2\nu)}} \quad (2)$$

where E, and ρ are the elastic modulus and material density, respectively. Using the calculated elastic wave speed with a 6 mm thick specimen, the elastic wave will reach the back surface in 1.03 μs. If the projectile and target are of the same material, identical waves will simultaneously propagate in both. The projectile will stay in contact with the specimen until the elastic wave in the projectile reflects off of the free surface and returns to the contact surface. The projectile and target will remain in contact for the time duration, $t_{Contact}$, determined as [13]:

$$t_{Contact} = \frac{2L_P}{C_{Elastic}} \quad (3)$$

where L_P is the projectile thickness. Since the projectile is half the thickness of the target specimen, they will separate in the same time the elastic wave reaches the back of the target, at 1.03 μs.

Each of the stress–time curves shown in Fig. 3 will be compared to that obtained numerically as will be detailed in a later section, for the same impact condition and will be used as a reference for obtaining particle velocity at the impact surface. Simulated particle velocity of the target impact surface will be used as an input into analytical constitutive equations formulated as the basis of the

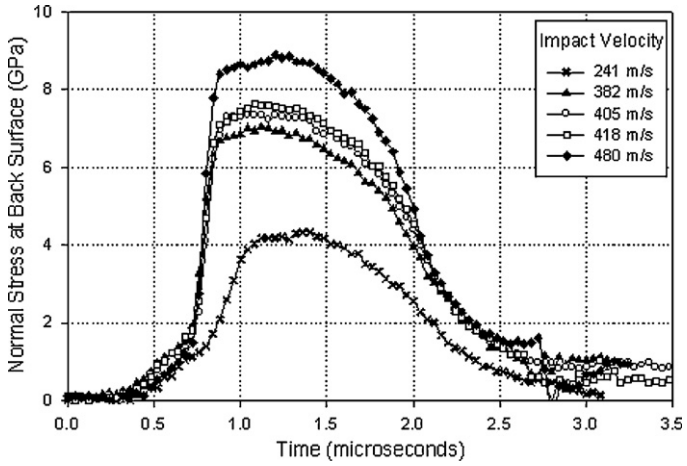

Fig. 3. Impact stress data recorded at the back surface of target disk.

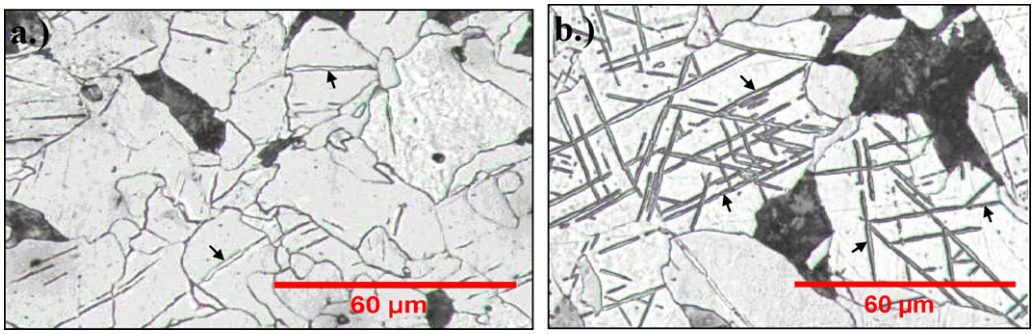

Fig. 4. Example of optical micrographs of post-impact steel specimens: (a.) 7 GPa peak stress yielding 3.4% twins, (b.) 9 GPa peak stress yielding 4.3% twins. Lighter grains are α-ferrite, and darker grains are pearlite; black arrows indicate deformation twins.

Johnson and Rohde, in order to calculate twin volume fraction as a function of local shear stress and time.

3. Experimental results

Post-impact target specimens show that plastic deformation took place in the impacted area and back surface as accompanied with an increase in total diameter of the target disk. The area of impact was discolored suggesting a large and rapid increase in temperature on the front surface during impact. Specimen surfaces were ground flat using a surface grinder under coolant, and polished and etched. Optical microscopy was conducted on post-impact test specimens and the results show the presence of mechanical twins within the α-ferrite grains; see Fig. 4. Micrographs of the cross-section just below the impact surface showed a lack of twins, which suggests that the temperature rise was high enough to suppress twin formation in the contact region.

Results of these optical micrographs show that all of the twins are of lenticullar shape, which is indicative of the mechanism by which the twins form. The majority of the grains have parallel twins extending between grain boundaries. However, there are also large amounts of twin–twin interaction in which twins terminate at other twins, or continue through the intersections, which suggests formation on multiple planes [14]. Volume fraction of the twins was calculated using ASTM E562-05, standard test method involving systematic manual point count method [15]. This count provides an average estimation of twin volume fraction which was correlated to impact stress, as shown in Table 1. Fig. 5 shows that macro hardness is also positively correlated to impact stress.

The increase in hardness, which indicates an increase in yield strength of the material, can be attributed to strain hardening [16], and to presence of twin–matrix interfaces, which provide additional barriers for further dislocation slip. There may exist a unique relationship between the twinning and hardness properties, however, since hardness also increases in the absence of twinning, no attempt has been made in this study to examine the unique relationship between hardness and twinning.

4. Numerical and analytical analysis

The analysis of the impact process will be carried out first by calculating the particle velocity for each impact condition. This velocity will then be utilized to calculate the corresponding deformation field and corresponding twin volume fraction.

Table 1
Peak impact stress and measured twin volume fraction.

Impact stress (GPa)	0.00	4.34	7.05	7.63	7.30	8.90
Mean twin V_f (%)	0.00	1.93	3.38	3.73	4.05	4.16

4.1. Particle velocity simulation

Dynamic-explicit finite element simulation was used to model plate impacts. Simulation of impact conditions provides knowledge of impact wave parameters as well as a description of the blast related stress distribution within the impacted steel. Input parameters for boundary and loading conditions are obtained from experimental procedures. From the simulation, the longitudinal stress distribution is matched with experimental stresses recorded. Once good correlation exists, particle velocity at the impact surface is extracted from numerical results and used as an input for analytical modeling of twin volume fraction as a function of impact loading. In order to obtain stress histories in accordance with experimental results, parameters for a rate dependent model were required. For this purpose, the Johnson–Cook (JC) constitutive model [17] was used to express the equivalent Von-Mises tensile flow stress as a function of the equivalent plastic strain, strain rate, and temperature. This stress is expressed as [13,17]:

$$\sigma = \underbrace{(A + B\varepsilon^n)}_{\text{Strain hardening}} \underbrace{\left[1 + C \ln\left(\frac{\dot{\varepsilon}}{\dot{\varepsilon}_0}\right)\right]}_{\text{Strain rate effect}} \underbrace{\left[1 - \left(\frac{T - T_r}{T_m - T_r}\right)^m\right]}_{\text{Temperature dependency}} \quad (4)$$

where σ is the Von-Mises tensile flow stress, which is the applied stress in the loading direction for the uniaxial tensile test case; ε is the equivalent plastic strain, which equals the strain in the loading direction for the uniaxial tensile test case; A, B and n are material constants to characterize the strain hardening behavior of the material; C is the material constant to describe the strain rate effect; m is the material constant to describe the temperature dependency. Values for material constants, Table 2, were optimized

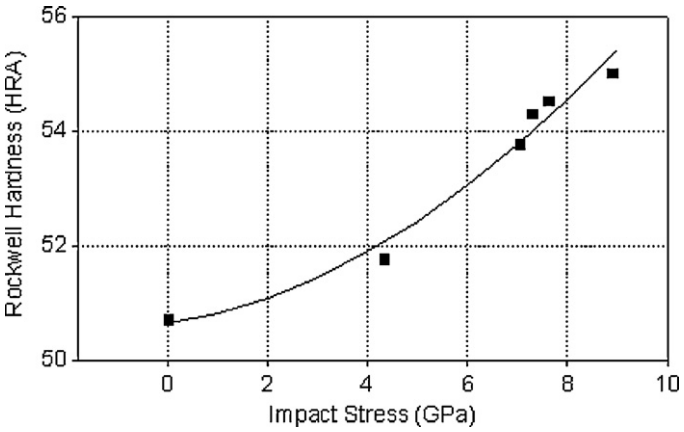

Fig. 5. Post-impact macro hardness (measured in Rockwell A scale with a major load of 60 kg) as a function of impact stress.

Table 2
Material properties and JC model constants for use in finite element simulation.

Young's modulus	Poisson's ratio	Density	Inelastic heat fraction	Specific heat
200 GPa	0.3	7850 kg/m^3	0.864	0.465 kJ/(kg K)
A	*B*	*C*	*n*	*m*
348	900	0.032	0.434	1

using a room temperature stress––strain curve of the as received material obtained from the work of Maciejewski et al. [16]; see Fig. 6.

Once the parameters for Eq. (4) are optimized, simulation of the plate impact is preceded. To obtain comparable σ_{HEL} during simulation, the constant *A* is adjusted from the static to the dynamic yield strength of the material. In this simulation, symmetry of the impacted test specimen permits simulation of only one quarter of the specimen, as illustrated in Fig. 7a; however, model boundary and loading conditions replicate that of the actual experiment, as illustrated in Fig. 7b. Step time period was 3 μs and included adiabatic heating effects. The model was symmetrically bounded on edges to prevent rotation and translation on the cross-sectional areas. The displacement and rotation of the surface of the backing plate was fixed in the axial direction corresponding to experimental setup. The temperature of the parts and the velocity of the projectile were defined as a predefined field. The mesh is standard hex type element CD38R with 12,416 and 1,848 elements in the target and flyer plate, respectively, and is approximately 1 mm × 1 mm on the surface and refined to 0.375 mm in the axial direction.

Numerical stress history of the target specimen during impact shows comparable profiles to experimental impact results. In this profile, three important components which must be captured accurately, pressure rise time, impact duration, and maximum stress, all exhibit good fit with experimental data. Fig. 8 shows numerically generated stress profiles during impact at the back surface of the target specimen compared with experimental results.

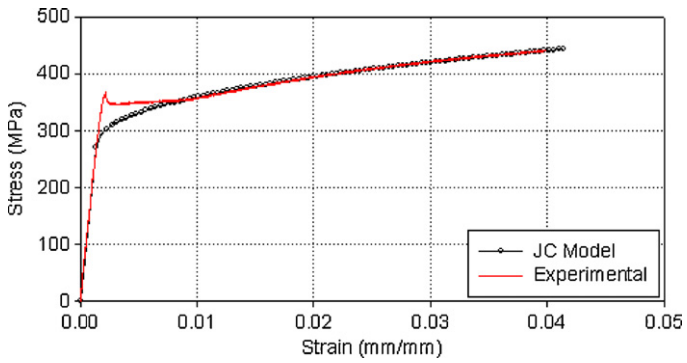

Fig. 6. Stress–strain curve of as received material plotted with JC model output. The curve was obtained at room temperature with a strain rate of 50^{-6} s^{-1}.

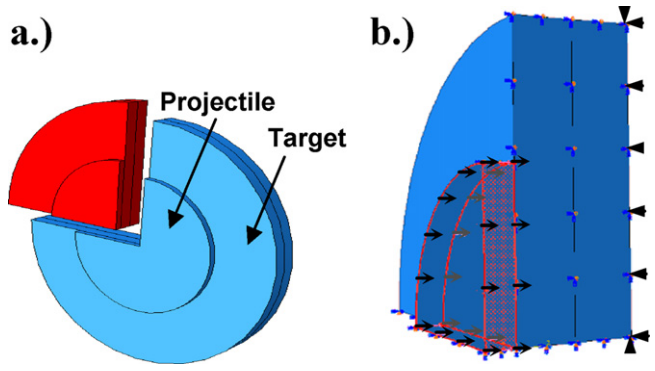

Fig. 7. (a.) Quarter plate model of axis-symmetrical target disk, and (b.) predefined velocity field imposed on projectile and fixed back boundary conditions on target.

Results show good correlation between rise time, peak stress, and σ_{HEL} amplitude. Linear and quadratic bulk viscosity parameters in the dynamic explicit step were adjusted in order to reduce noise in the numerical solution. Furthermore, the linear and quadratic bulk viscosity parameters damp high frequency ringing and smear the shock front across several elements to prevent collapse under high velocity gradients. Once good agreement between numerical and experimental stress–time curves is achieved, the simulated maximum particle velocity at the front surface of the specimen can be used as an input for calculation of twin volume fraction. An approach to carry out these calculations is described in the following section.

4.2. Twin volume fraction calculation

The twin region can be simply described as an area of stacking faults enclosed by partial dislocations. Two ways in which this can occur are discussed by Wasilewski [18]. Wasilewski suggests that twins can form by progressive shear of the parent lattice or by a close atomic shuffle within the lattice, both of which will end in the same arrangement within the twinning planes; Fig. 9. Twinning by progressive shear of the parent lattice will produce a shear offset, of which plastic deformation results, Fig. 9a, while a local rearrangement or shuffle will produce no shear offset, Fig. 9b. It is assumed that formation of the twin by homogeneous shear will produce a shear offset equal to *kh*, where *k* is the strength of the simple shear, also known as the *twinning shear*, and *h* is the average thickness of the twin lamella. For bcc crystals the twinning is most readily formed on the {1 1 2} planes in the (1 1 1) direction which has a twinning shear equal to $1/\sqrt{2}$ [6]. The two modes can be distinguished by observation of the shape of the twins formed. Twins by shear will be lenticullar in shape while those created by shuffle will be prismatic [18]. Based upon the characteristic lenticular shape of the twins formed in this study, they are assumed to be produced by progressive shear of the parent lattice, as in opposition to the theory of atomic shuffle.

From the works of Wasilewski [18] and Johnson and Rohde [6], it is inherent that twins form by local rearrangement of atoms resulting in a shear offset, as opposed to local shuffling. In order to analytically predict twin volume fraction, these two points are considered and a modified form of a deformation model based on the work of Johnson and Rohde [6] was therefore applied here. This deformation model incorporates slip and twinning mechanisms previously described [18–20] and will be used to calculate twin volume fraction in the material for the given loading conditions. The assumptions and observation from these previous studies are described in the constitutive model in which total plastic strain is composed of both dislocation slip and deformation twinning, and the twin volume fraction and growth rate are functions of corresponding shear stress. The dynamic response and deformation twinning of low carbon steel under impact loading is described by

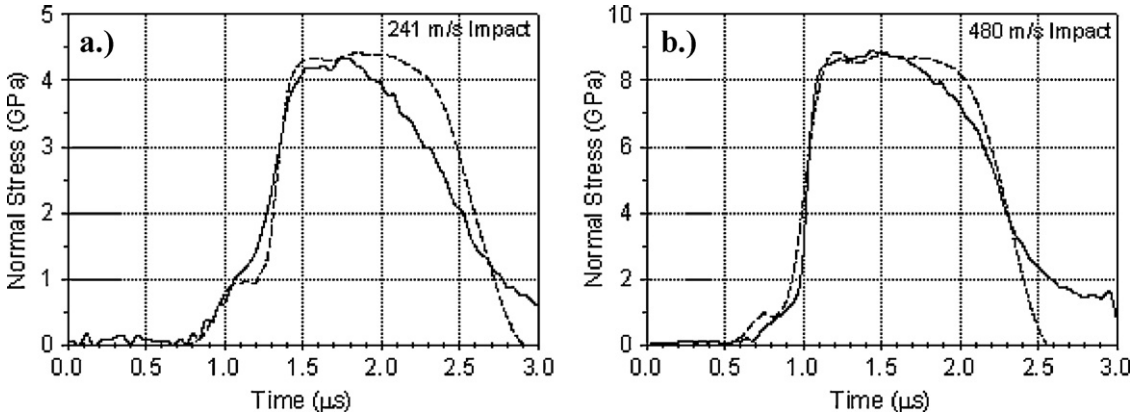

Fig. 8. Experimental (solid line) and numerical (dashed line) stress history data matching for two impact cases. Graph legends pertain to projectile velocity.

the laws of mass and momentum conservation, which are written as:

$$\frac{\rho_0}{\rho^2}\frac{\partial \rho}{\partial t} + \frac{\partial u}{\partial X} = 0 \tag{5}$$

$$\rho_0 \frac{\partial u}{\partial t} + \frac{\partial \sigma}{\partial X} = 0 \tag{6}$$

where ρ_0 is initial density, ρ is an evolved density, and u is particle velocity during impact at time t at a distance of X from the impact surface. The stress, σ, component can be defined by a contact pressure P, and shear stress τ, and is expressed as:

$$\sigma = P + \frac{4}{3}\tau \tag{7}$$

where

$$P = \rho(C + Su)u \tag{8}$$

and

$$\dot{\tau} = \mu(\dot{\varepsilon}_t - 2\dot{\gamma}) \tag{9}$$

where μ is shear modulus, C and S are wave speed constants, and ε_t is total strain in the wave direction and is given by:

$$\varepsilon_t = 1 - \frac{\rho_0}{\rho} \tag{10}$$

γ is the plastic shear strain on the plane of maximum shear stress described as the summation of slip and twinning strains:

$$\gamma = \gamma_s + \gamma_{tw} \tag{11}$$

Plastic strain due to twinning, and that due to slip are expressed as:

$$\gamma_{tw} = k(\alpha - \alpha_0) \tag{12}$$

$$\gamma_s = \frac{1}{2}\varepsilon_t - 2k\alpha - \alpha_0 - \frac{\tau_s}{\mu} \tag{13}$$

respectively, where k is twinning shear, α is the volume fraction of twins, α_0 is initial twin volume fraction, and τ_s is the shear stress required for slip. Volume fraction of twinned material is given by:

$$\alpha = \left(\alpha_0^{1/m} + \frac{1}{t_c}\int_0^t \nu(\tau)\,dt\right)^m \tag{14}$$

where t_c is characteristic time, which is a constant controlling the rate of twin density, and $m = 3$ is for growth of twins both through the thickness and radial directions. The dimensionless growth rate of twins, $\nu(\tau)$, is expressed as:

$$\nu(\tau) = \frac{\tau}{\tau_T} - 1 \quad \tau \geq \tau_T \tag{15}$$

where τ_T is shear stress required for twinning. This set of equations provides a method of calculating twin volume fraction as a function of shear stress. The results of this model in terms of average twin volume fraction versus impact stress are compared with experimental results, and are shown in Fig. 10.

Analytical model predictions show similar trends to experimental measurements for the given stress range. The linearity of the experimental and calculated data in Fig. 10 apparently deviates

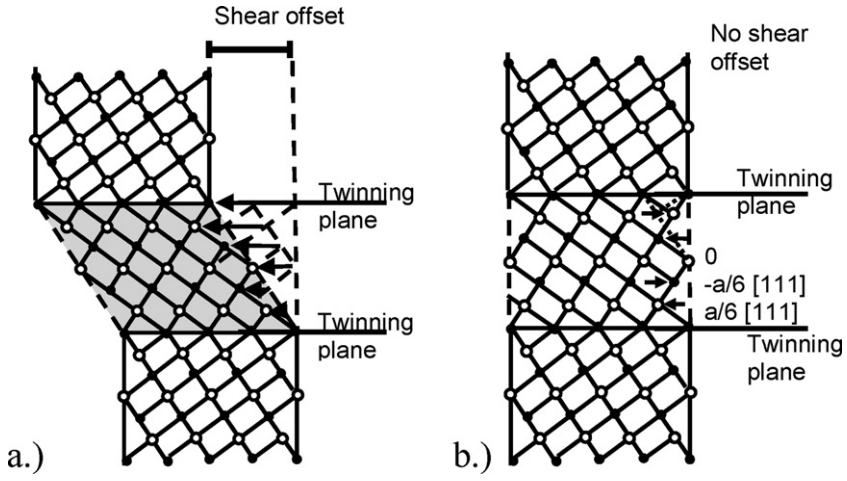

Fig. 9. (a.) Twin formation by progressive shear of the parent lattice, and (b.) twin formed by successive alternating "shuffle" of atoms by sequence $+a/6[1\ \bar{1}\ 1]$, $-a/6[1\ \bar{1}\ 1]$, 0 [18].

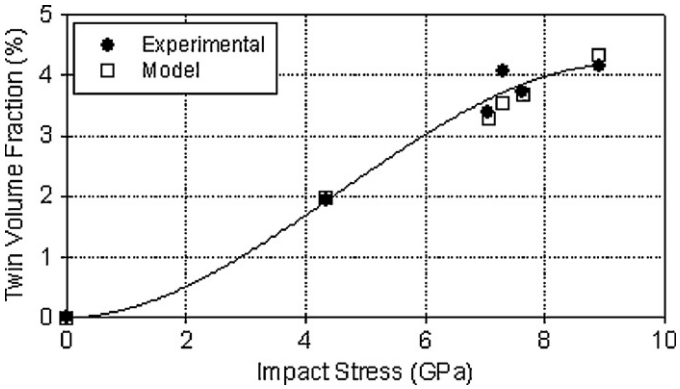

Fig. 10. Comparison of experimentally measured and analytically computed twin volume fraction within α-ferrite grains as a function of impact stress.

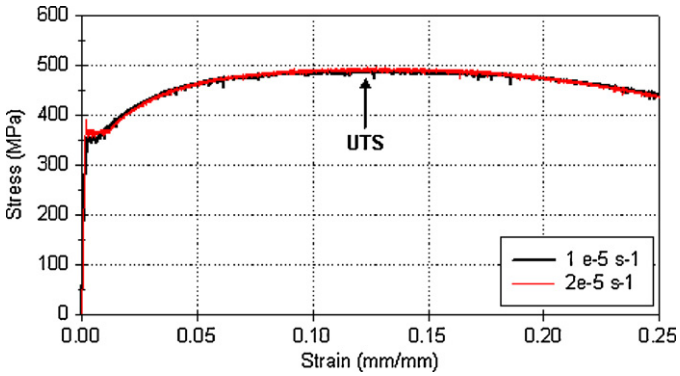

Fig. 12. Stress–strain curves of as-received material tested at strain rates of 10^{-5}/s and 20^{-5}/s.

from this trend at higher stresses as the twin volume fraction seems to saturate in the material, or other deformation mechanisms begin to dominate. While the relationship between impact stress and twin volume fraction may be satisfied within the given conditions, shear banding and phase transformation have been observed to occur at extremely high pressures [4,21], and the criteria may no longer be valid. Further study of the material at higher stresses and strain rates are underway by the authors in order to extend the deformation criterion and set limits for its applicability.

5. Post-impact residual strength

The influence of twin volume fraction on the residual strength of the material is examined through strain rate controlled monotonic tensile tests and has been compared to the response of the as-received condition. For this purpose, post-impact steel discs were ground and polished flat to a nominal thickness of 3 mm and cut into dog-bone specimens. Geometry and dimensions of the specimen as being cut from the impacted disc are illustrated in Fig. 11. Testing was carried out at room temperature using a servo hydraulic mechanical test system and strain values were recorded using a knife edge extensometer mounted in the gauge section of the test specimen. Testing of as-received material was carried out at two strain rates; 10^{-5}/s and 20^{-5}/s. Results show no strain rate dependency at this rate and temperature. All post-impact specimens were tested at 20^{-5}/s.

It was observed that as-received specimens began necking at 20% strain, while the post-impact specimens began necking in the range of 10–20%, depending on the impact stress history. Engineering stress–strain curves for the as-received material are presented in Fig. 12. These curves show clear upper and lower yield points, Lüders extension [22] and serrated plastic flow resembling characteristics of Portevin–Le Châtlier effects [23]. Despite the serrated characteristics, the amplitude of serration is minimal in comparison to the magnitude of the general stress level, and is considered insignificant in the overall analysis of the curves. Engineering stress–strain curves of the post-impact tensile specimens, categorized by impact velocity and volume fraction of twins, are presented in Fig. 13.

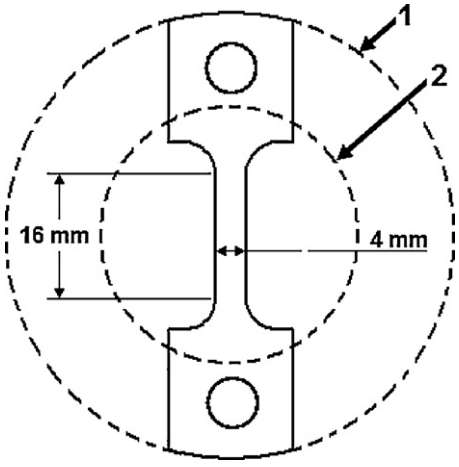

Fig. 11. Tensile specimen (3 mm thick) cut from impact region **2**, of target disk **1**.

Post-impact mechanical response of the material showed an increase in yield strength and slight increase in the ultimate strength, and a decrease in the work hardening. A comparison between yield and UTS for different twin volume fractions is shown in Fig. 14.

This figure shows that as twin volume fraction increases, the yield stress approaches the ultimate strength of the material. The convergence of these curves indicates that the plastic hardening characteristics are becoming less prominent. Figs. 14 and 15 suggest that an increase in twin volume fraction results in a decrease in the ability of the material to store defects during post-impact plastic deformation, which is represented by the loss in work hardening [21] and in the loss of available strain energy up to UTS. Furthermore, quantitative and qualitative interpretation of mechanisms governing elastic–plastic response and instability of the material can be made by comparing the as-received and post-impact stress–strain characteristics.

The as-received and the post-impact stress–strain curves both exhibit serrated flow characteristics which have been observed and reported in low carbon and stainless steels [22,24]. Post-impact specimens lack an upper and lower yield point and are characterized by presence of serrations. These serrations can occur in the event of an increase in dislocation density or velocity or both [25]. This increase can be attributed to dislocations within deformation bands locking and unlocking and can be distinguished by three different profiles; type-A, type-B, and type-C [25,26], as illustrated in Fig. 16. Type-A serrations are characterized by periodically spaced yield points which increase in size and spacing with further straining. This process is controlled by the formation and propagation of deformation bands along the gauge section [26]. Increases in stress are due to large solute atmospheres which prevent unpinning of dislocations, while the creation of new dislocations suddenly decreases the stress. Each successive deformation band requires higher stress to activate. Type-B serrations are characterized by quickly fluctuating peaks and valleys lying along the general level of the stress–strain curve. In this case, in contrast to type-A, the serrations are the result of the propagation of deformation bands rather than formation of new bands. In order to maintain the applied strain rate, an increase in dislocation density,

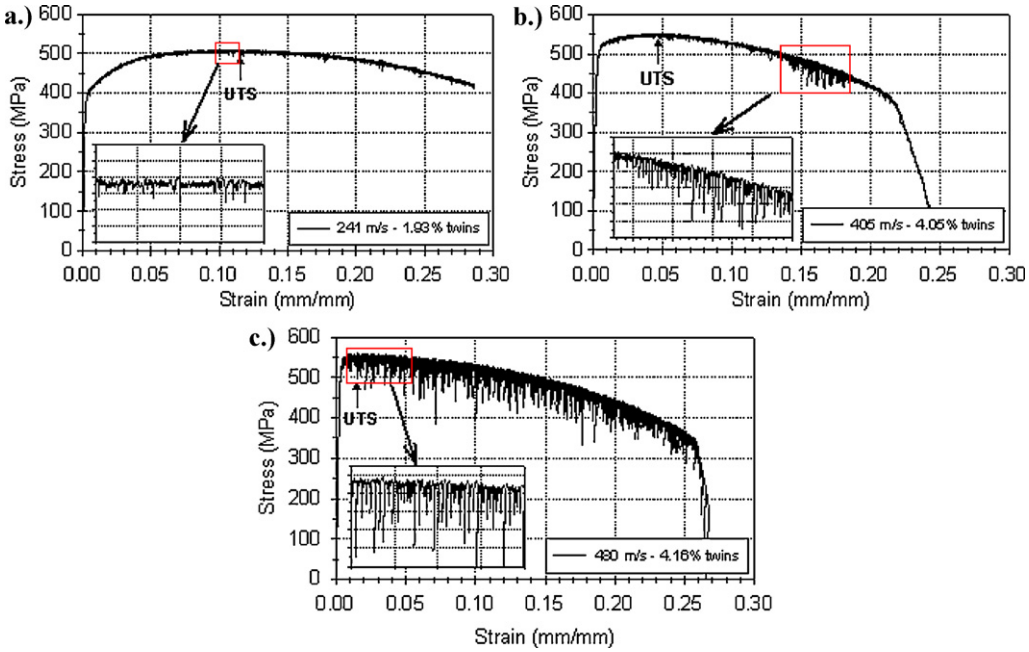

Fig. 13. Stress–strain curves of post-impact steel specimens. Graph legends pertain to projectile velocities at which the steel was impacted and resultant twin volume fraction. Inset graph shows detailed view of serration characteristics.

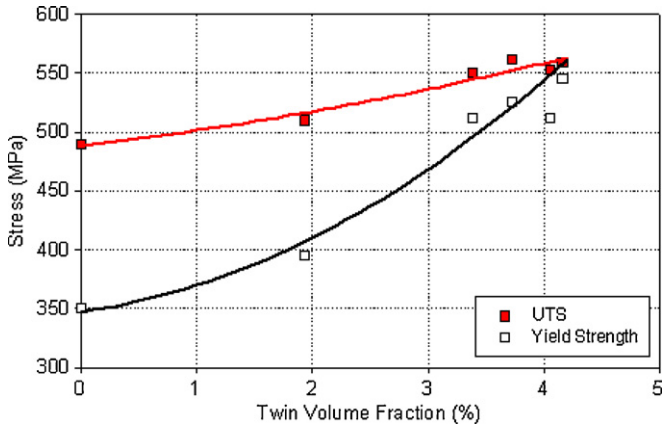

Fig. 14. Ultimate tensile strength and yield stress of post-impact tensile specimens as a function of twin volume fraction.

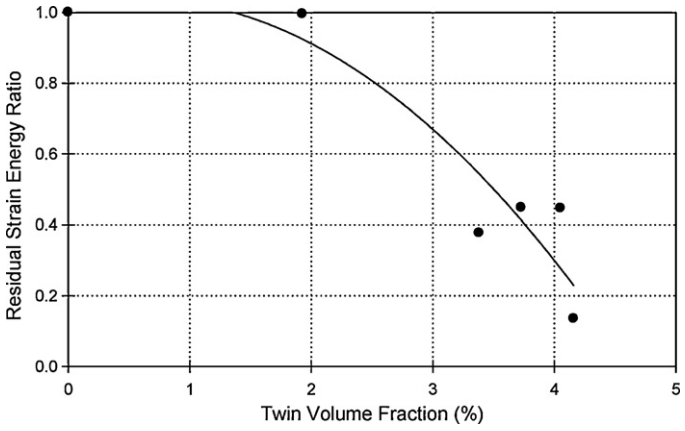

Fig. 15. Residual strain energy ratio versus twin volume fraction. The ratio is in reference to the as-received condition with no twins. Strain energy is measured as area under the curve up to strain at UTS.

and in turn, a decrease in average dislocation velocity results in segregation of solute atoms. The slow moving dislocations become locked rapidly until the stress increases and breaks the dislocation free again, thus allowing the band to propagate. This process continues within the deformation band until it has run through the entire gauge section or has encountered another band [25]. Type-C serrations are characterized by distinct yield drops occurring below the general level of the stress–strain curve. This process is controlled by unlocking of pinned dislocations. Inhomogeneous deformation due to stress concentrations created at barriers, such as grain or twin boundaries, result in localized regions of a higher strain rate. This creates additional drag on the atmosphere of dislocations and in turn, frees dislocations and reduces the stress. The sudden availability of mobility decreases the average dislocation velocity in the deformation band and sets up a condition for solute atoms to relock the dislocations and repetition of the process [25].

The type-C load drops, as well as the general softening behavior characterizing the post-impact stress–strain curves can be attributed to Sleeswyk's emissary dislocation mechanism [28]. As Fig. 4b shows, several of the twins, while lenticullar shaped, have blunted ends. This is evidence that the twinning shear is accommodated by slip in the matrix [24]. The incoherent twin boundary can be schematically visualized in Fig. 17. During tensile testing, slip in the matrix can emanate from available dislocations which make up the incoherent twin boundary; Fig. 17(a). This dislocation boundary supports a high energy configuration surrounding the twin. As further straining continues, the matrix accommodates plastic deformation by slip of these dislocations upon dissociation of every third dislocation:

$$\frac{1}{6}[1\,1\,1] \rightarrow \frac{1}{2}[1\,1\,1] - \frac{1}{3}[1\,1\,1]$$

as shown in Fig. 17(b). A 1/2 [1 1 1] total dislocation glides away from the twin, leaving behind a 1/3 [1 1 1] complementary dislocation, and drastically lowers the configuration energy. Thus, as further plastic deformation continues, the energy is reduced locally allowing for dislocation pile-ups to break through the twin boundary, as can be seen in the stress reduction of Fig. 13c. If the matrix is

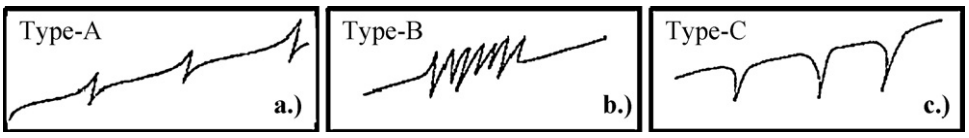

Fig. 16. Typical segments of a stress–strain profile with (a.) type-A, (b.) type-B, and (c.) type-C serrations.

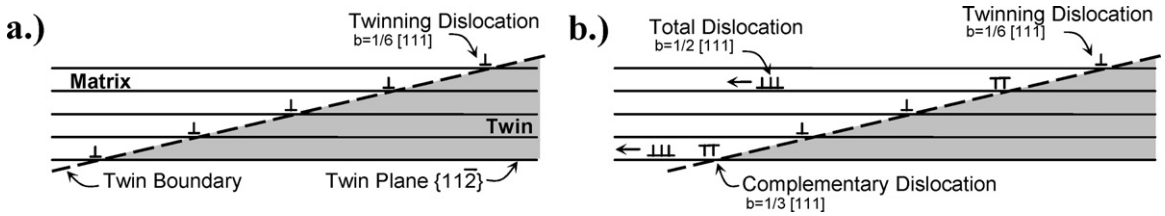

Fig. 17. (a.) Incoherent twin boundary composed of twinning dislocations on {1 1 2} planes, and (b.) dissociation of twinning dislocation as the matrix accommodates slip [24].

not able to accommodate the shear, then a crack may develop in the twin boundary region. The cracking can be seen in Fig. 18, as they are formed both along the ferrite–pearlite interface, and within the ferrite grains [27], both which occur parallel to the twinning direction. This suggests that the presence of twins in the microstructure influences the not only the elastic–plastic response, but also the characteristics of the failure mechanism.

The as-received tensile curves show type-B serrations occurring from the onset of yield through the entire plastic stress–strain curve. Post-impact specimens with less than 4% twins also exhibit type-B serrated flow with a random minority of type-C load drops, as shown in detail in the inset of Fig. 13a. Fig. 13b shows, as the volume fraction of twins increases to 4%, the stress–strain curve transitions from type-B to type-C serrations upon further straining [25]. A detailed view of the type-B to type-C transition is shown in the inset of Fig. 13b. Although this transition is after the UTS, it still acts as an indication that twin interactions are becoming a dominant mechanism for locking mobile dislocations. As the volume fraction of twins increases further, as shown in Fig. 13c, the majority of the serrations are of type-C.

Since type-C serrations occur from unlocking of pinned dislocations, the transition from B to C could suggest that the material has reached a point where all stored dislocations are locked up due to the presence of twinned regions [21]. During post-impact straining, the networks of locked dislocations between twinned regions break free, causing successive load drops. This change in stress–strain characteristics suggests that the material has transitioned to a point of instability when 4% or more twins exist in the microstructure.

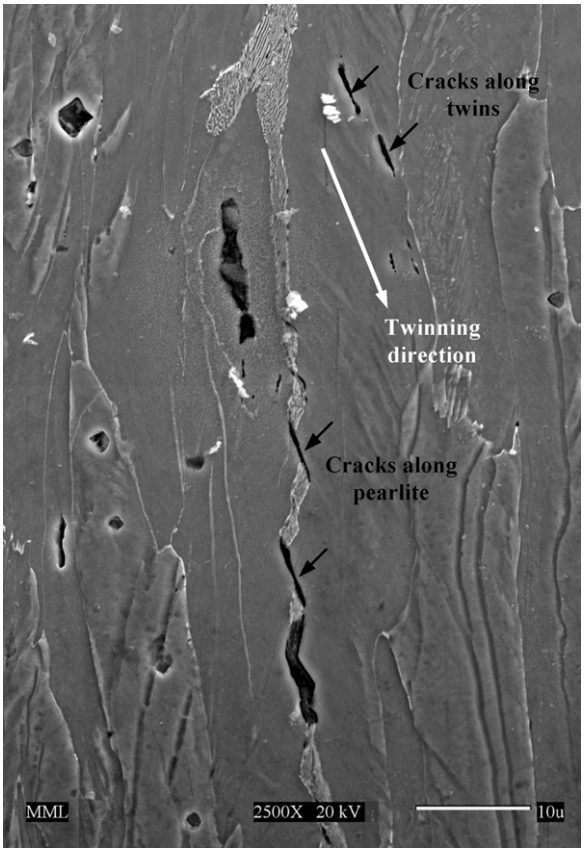

Fig. 18. SEM micrograph of necked region in post-impact tensile specimen. Cracking occurred along the ferrite–pearlite and twinning interfaces during post-impact tensile testing. All of the cracks within this region are oriented in the twinning direction, suggesting that twins play a role during fracture.

6. Conclusions

The objective of the study is to present a correlation between high rate impact and microstructure variation of low carbon steel. Five plate impact experiments were carried out and post-impact microscopy shows deformation mechanisms occurring during shock loading of low carbon b.c.c. steel. The coupling of numerical simulations and the analytical constitutive model acts as a tool for defining impact history and predicting post-impact microstructure. Results of this study can be briefly summarized as follows:

1. A direct and unique relationship between impact stress and volume fraction of twins has been experimentally established.
2. Microscopic observation of impact specimens indicate that slip and mechanical twinning are two competing deformation mechanisms occurring during high rate loading of low carbon steel. The lenticullar shape of the twins indicates that the twin formation mechanism is by progressive shear of the parent lattice. As impact stress increases, another twinning plane becomes active, and results in large amounts of intergranular twin–twin interactions.
3. Based on microscopic observations, an analytical twinning model aiming at predicting twin volume fraction incorporating both slip and twinning mechanisms has been applied and shown to accurately calculate twin volume fraction. This model was coupled with a rate dependent model implemented into numerical procedures and was capable of capturing deformation response and twin formation during impacts for the given stress range.

4. Quantitative analysis of the post-impact stress–strain curves clearly shows an increase in both yield and ultimate strength, which indicates an increase in stored dislocations in the microstructure as a result of impact loading. However, while the yield and UTS both benefit from shock loading, the available strain energy is drastically reduced; up to 87%. If this trend is extrapolated further, it will show that the yield and ultimate tensile strength converge, thus eliminating available energy.
5. It is apparent that as the shock loading is increased, new twinning planes are activated. Qualitative analysis provides insight into the dislocation-twinning interaction during plastic deformation. Low impacted specimens reveal small fluctuations in stress–strain response representing that of type-B serrations. At higher impact levels, the presence of multiple twinning planes and twin–twin interactions results in the transition of type-B serrations to type-C load drops during plastic deformation. This suggests that twin–twin interactions play a significant role in controlling plastic deformation, which is responsible for instability within the microstructure.
6. The twins play an important role in the direction of cracking during failure. They provide new interfaces at which cracks may initiate and propagate, and also control the direction of crack propagation.

Acknowledgment

This project has been funded by the Department of Homeland Security Center of Excellence: Explosives Detection, Mitigation, and Response at the University of Rhode Island.

References

[1] J.Y. Richard Liew, Journal of Constructional Steel Research 64 (2008) 854–866.
[2] J.E. Field, S.M. Walley, W.G. Proud, H.T. Goldrein, C.R. Siviour, International Journal of Impact Engineering 30 (2004) 725–775.
[3] O. Gregory, J. Oxley, J. Smith, M. Platek, H. Ghonem, E. Bernier, M. Downey, C. Cumminskey, Materials Characterization 61 (3) (2010) 347–354.
[4] D. Firrao, P. Matteis, G. Scavino, G. Ubertalli, M.G. Ienco, G. Pellati, P. Piccardo, M.R. Pinasco, E. Stagno, R. Montanari, M.E. Tata, G. Brandimarte, S. Petralia, Materials Science and Engineering A 424 (2006) 23–32.
[5] T. De Resseguier, M. Hallouin, Journal of Applied Physics 84 (4) (1998) 1932–1938.
[6] J.N. Johnson, R.W. Rohde, Journal of Applied Physics 42 (11) (1971) 4171–4182.
[7] J.W. Taylor, Journal of Applied Physics 36 (10) (1965) 3146–3150.
[8] S.A. Atroshenko, N.S. Naumova, S.A. Novikov, International Journal of Impact Engineering 33 (2006) 62–67.
[9] T. Smida, J. Bošanský, Materials Science and Engineering A 287 (2000) 107–115.
[10] L.E. Murr, M.A. Meyers, Acta Materialia 45 (1) (1997) 157–175.
[11] M.A. Meyers, O. Vöhringer, V.A. Lubarda, Acta Materialia 49 (2001) 4025–4039.
[12] M.A. Meyers, D.J. Benson, O. Vöhringer, B.K. Kad, Q. Xue, H.-H. Fu, Materials Science and Engineering A 322 (2002) 194–216.
[13] V. Panov, Ph.D. Thesis, Cranfield University, 2005.
[14] S. Mahajan, Metallurgical Transactions A 12A (1981) 379–386.
[15] L. Jiang, J. Jonas, R. Mishra, A. Luo, A. Sachdev, S. Godet, Acta Materialia 55 (2007) 3899–3910.
[16] K. Maciejewski, Y. Sun, O. Gregory, H. Ghonem, International Journal of Steel and Iron Research (2011), in press.
[17] G.R. Johnson, W.H. Cook, Proceedings of the Seventh International Symposium on Ballistic, La Hague, Netherlands, 1983, pp. 541–547.
[18] R.J. Wasilewski, Metallurgical Transactions 1 (1970) 2641–2643.
[19] J.W. Christian, S. Mahajan, Progress in Materials Science 39 (1995) 1–157.
[20] S. Mahajan, Acta Metallurgica 23 (1975) 671–684.
[21] L.M. Dougherty, E.K. Cerreta, E.A. Pfeif, C. Trujillo, G.T. Gray, Acta Materialia 55 (2007) 6356–6364.
[22] E. Pink, S. Kumar, Materials Science and Engineering A 201 (1995) 58–64.
[23] K. Renard, S. Ryelandt, P.J. Jacques, Materials Science and Engineering A 527 (2010) 2969–2977.
[24] Reed-Hill, E. Robert, Physical Metallurgy Principles, 2nd ed., Nostran, New York, 1973, pp. 611–660.
[25] D. Fahr, Analysis of stress–strain behavior of type 316 stainless steel, ORNL/TM-4292, 1973, Oak Ridge National Laboratory Report.
[26] P. Rodriguez, Bulletin of Material Science 6 (4) (1984) 653–663.
[27] N. Narasaiah, K.K. Ray, Materials Science and Engineering A 392 (2005) 269–277.
[28] A.W. Sleeswyk, Acta Metallurgica 10 (1962) 803–812.